Analysis of Phase Error Effects on Stripmap SAS

Daniel A. Cook, *Member, IEEE*, and Daniel C. Brown

***Abstract*—It is often of interest to consider how uncompensated platform motion can degrade the ideal point scatterer response (PSR) of a synthetic aperture sonar (SAS). This information can be used to shape the design of the sonar itself as well as that of the platform carrying it. Also, knowledge of how certain types of motion affect a SAS image can reduce the time spent in troubleshooting motion estimation and compensation schemes. In the field of spotlight-mode synthetic aperture radar (SAR), the effects of phase errors across the synthetic aperture are well documented (for example, Chapter 5 of Carrara *et al.*, 1995). The counterpart problem for the stripmap mode is less well developed in the literature. This paper explores the effects of uncompensated phase errors on stripmap imagery and shows that, under certain conditions, they are similar to those for spotlight mode processing.**

***Index Terms*—Motion compensation, motion estimation, phase error, spotlight, stripmap, synthetic aperture, synthetic aperture radar (SAR), synthetic aperture sonar (SAS).**

I. Introduction

UNDERSTANDING how specific types of phase errors degrade the quality of focus is fundamentally important to the field of synthetic aperture sonar (SAS). Such an analysis has existed for some time in the spotlight synthetic aperture radar (SAR) literature, and is best summarized by Chapter 5 of Carrara *et al.* [1]. However, virtually all SASs operate using the stripmap modality. Some analysis of stripmap phase errors exists in the SAR literature [2]–[7], but the coverage is not as thorough or consistent as the treatment of spotlight errors. The goal of this paper is to extend and summarize the coverage of phase error effects for stripmap mode synthetic aperture imaging. This is accomplished by analyzing several canonical phase error types within a common mathematical framework based on the stripmap imaging model for a single point scatterer.

From a qualitative standpoint, the ability to associate a given type of phase error with a characteristic degradation of the point scatterer response (PSR) is useful in diagnosing image quality problems when troubleshooting SAS processing algorithms. For example, high-frequency random phase errors result in an overall loss of contrast (i.e., peak-to-average-sidelobe ratio), but they do not degrade the resolution (−3-dB width of the PSR mainlobe). On the other hand, periodic errors tend to create replica, or ghost, copies of the PSR.

Manuscript received December 12, 2006; revised June 22, 2007; accepted September 04, 2007. First published December 09, 2008; current version published August 05, 2009. This work was supported by the U.S. Office of Naval Research Code MIW32.

Guest Editor: P. E. Hagen.

D. A. Cook was with the Code HS11, Naval Surface Warfare Center, Panama City, FL 32407 USA. He is now with the Sensors and Electromagnetic Applications Laboratory, Georgia Tech Research Institute (GTRI/SEAL), Atlanta, GA 30332 USA (e-mail: daniel.a.cook@gmail.com).

D. C. Brown was with the Code HS11, Naval Surface Warfare Center, Panama City, FL 32407 USA. He is now with the Sonar Research and Development Department, Applied Research Laboratory, The Pennsylvania State University, State College, PA 16804-0030 USA.

Digital Object Identifier 10.1109/JOE.2007.907935

The quantitative analysis of phase error effects is also applicable to the design process. An error budget can be constructed that allows the system designer to allocate resources in ways that will reduce the most serious forms of degradation. For example, knowledge of a sonar's phase error tolerances can be used to choose the most cost-effective sensors among those capable of measuring vehicle motion with the necessary accuracy. Similar error budgets can be used for developing the processing algorithms, tuning any relevant vehicle control software, and optimizing the operational procedures for deploying the SAS.

II. Stripmap Versus Spotlight Phase Errors

Before discussing the effects of stripmap phase errors, it is worthwhile to discuss how its phase error model differs from the spotlight case. First, the degraded spotlight PSR is given by the ideal PSR convolved with the Fourier transform of the corrupting phase function. This result is based on the tomographic paradigm of spotlight imagery as elucidated by Jakowatz *et al.* in their well-known book [8] and by Munson *et al.* [9]. Briefly, the key features of the tomographic model are as follows: 1) the physical sensor has a narrowbeam such that the wavefront curvature is negligible over the illuminated patch; 2) the transmitted signal is narrowband so that time delays due to platform motion ΔR can be approximated by a multiplicative phase shift term $\exp\{-j2k_0\Delta R\}$; and 3) the received temporal signals are pulse compressed and Fourier transformed into the frequency domain. This is often accomplished by transmitting linearly swept frequency-modulated (LFM) chirp waveforms using "deramp" or "stretch" processing upon reception, which performs pulse compression and Fourier transformation simultaneously [10]. The consequence of 1) and 3) and the Fourier slice theorem [9], [11] is that each transmission/reception along the synthetic aperture gives a slice of the 2-D Fourier transform of the scene. Item 2) enables the delay term to be treated as a complex constant for each cross-range position, and hence, it can be factored out of the Fourier transform operation. In other words, the cross-range phase error history is multiplied with the 2-D Fourier transform of the imaged scene. When the scene is reconstructed by Fourier transformation, often via polar formatting, the transform of the phase error function is related to the cross-range dimension of the scene through convolution [8].

Stripmap data, on the other hand, cannot be considered to have been collected directly in the 2-D Fourier domain. Assuming narrowbeam and narrowband operation as before, the cross-range phase error history is multiplied with the cross-range signal history in the spatial domain. Thus, the spatial frequency spectrum of the received data is related to that of the phase error through convolution, not multiplication as for the spotlight case. In spite of the fact that stripmap phase errors operate under a different mechanism compared to spotlight mode, it is shown in Sections III and IV that under certain constraints the PSR degradation is similar for both cases.

The difference between the spotlight and stripmap phase error models has been observed in the autofocus literature [12]. Very successful spotlight-mode autofocus techniques exist [1], [8]. However, to date, the goal of developing robust stripmap autofocus schemes has proven more elusive, although a number of techniques are being used successfully. The effectiveness of spotlight autofocus can be attributed to the fact that PSR distortion is the same for all scatterers in a scene. On the other hand, stripmap PSR distortion is generally spatially variant, as each scatterer in a stripmap image "sees" a different phase error history depending on its location. The problem of stripmap SAS autofocus is discussed by Hawkins [13] and Callow [14].

III. Origin of Stripmap Phase Error Effects

For short-range SAS systems designed to operate aboard autonomous underwater vehicles (AUVs) in the littoral environment, the primary source of phase errors is unwanted platform motion. Even when the motion has been estimated and compensated, residual phase errors inevitably remain in the data. In addition to motion-induced errors, phase errors might be introduced through hardware by a lack of proper calibration of the hydrophone array or by timing problems in the transmission or data acquisition systems. Fluctuations in the medium are another source of phase errors [15]. These errors become increasingly significant at long ranges, where the coherent integration time (i.e., the synthetic aperture) is longer and where the imaged scene is far removed from the local sound-speed measurements made onboard the vehicle carrying the SAS. This paper is primarily concerned with the effects of unwanted motion. Nevertheless, the analysis of Section IV is general and applies to all stripmap phase errors regardless of origin.

For narrowbeams, uncompensated motion in the range direction effectively only causes delay in the observed signal. After compensation, the residual delay error should not exceed a range resolution cell; otherwise, the synthetic aperture focusing will generally be poor. For this reason, the discussion is restricted to the simpler case of motion errors whose magnitude is less than a resolution cell. Such errors can be modeled as an additional phase term in the observed signal. The analysis is furthermore restricted to a single point scatterer located at $(x, y) = (x_0, 0)$, which then creates a planar geometry defined by the nominal sensor trajectory (coinciding with the y-axis) and the scatterer of interest. Within this plane, cross-range focusing can be thought of as a spatially varying 2-D correlation operation (see [13] and [16] for a thorough treatment of SAS imaging fundamentals). Here, the problem is treated as 1-D by assuming that the curvature of the hyperbolic range migration of the received signal is small or has been removed. The cross-range focusing operation then reduces to correlating the observed signal with the ideal signal. This operation is given by

$$\begin{aligned} f(y) &= \exp\{-j2kR'(y)\} \odot_y \exp\{-j2kR(y)\} \\ &= \int_{-L_{\mathrm{SA}}/2}^{L_{\mathrm{SA}}/2} \exp\{-j2kR'(u)\} \exp\{+j2kR(u-y)\}\, du \end{aligned} \tag{1}$$

where

$$R(y) = \sqrt{x_0^2 + y^2}$$

$$R'(y) = \sqrt{(x_0 - \epsilon(y))^2 + y^2}$$

L_{SA} is the length of the synthetic aperture, $\odot_y$ represents correlation with respect to the variable y, $k = \omega/c$, and $\exp\{-j2kR(y)\}$ is the ideal signal phase history from a single point scatterer. Because $\exp\{-j2kR(y)\}$ is an even function [since $R(y) = R(-y)$], the previous correlation operation can also be written as the following convolution:

$$\begin{aligned} f(y) &= \exp\{-j2kR'(y)\} *_y \exp\{+j2kR(y)\} \\ &= \int_{-L_{\mathrm{SA}}/2}^{L_{\mathrm{SA}}/2} \exp\{-j2kR'(u)\} \exp\{+j2kR(y-u)\}\, du \end{aligned} \tag{2}$$

where the symbol $*$ indicates convolution with respect to the subscripted variable. This fact is exploited in Section IV-F to study the effect of random phase errors on the PSR $f(y)$. In the previous expressions, the amplitude term due to the directivity pattern of the physical aperture is approximated by assuming it is equal to one inside the -3-dB beamwidth and zero otherwise. The quantity R is the ideal range (i.e., R is referenced to the nominal trajectory), R' is the actual range from the sensor to the scatterer at cross-range position $y = 0$, and ϵ represents an unwanted motion in the x-direction. In keeping with the small-magnitude error assumption, R' can be expanded about the point $\epsilon(y) = 0$ as follows:

$$\begin{aligned} R' &\approx R + \left.\frac{dR'}{d\epsilon}\right|_{\epsilon=0} \epsilon \\ &\approx R - \left(1 - \frac{y^2}{2x^2}\right)\epsilon \\ &\approx R - \epsilon \end{aligned} \tag{3}$$

where the last simplification is based on the condition that $y \ll x$. This is equivalent to assuming that the sensor has a narrowbeam, in which case the width of a given illuminated interval of y would be small compared to its range x. This also implies that the delay induced by the motion error is the same for all scatterers in the beam. (Otherwise, the delay is proportional to $\cos\theta$ for scatterers located at an angle θ relative to boresight.) Note also that the analysis is carried out only for a single frequency k_0. This is a suitable approximation for relatively narrowband systems. Wideband results can be obtained through superposition of the narrowband results as discussed in Section V.

Equation (3) allows the observed phase history from the right-hand side of (1) to be written as

$$\exp\{-j2k_0R'(y)\} \approx \exp\{-j2k_0(R(y) - \epsilon(y))\}. \tag{4}$$

This indicates that small motion errors simply introduce an additive phase distortion into the observed signal. This result can be used to make quantitative statements about the behavior of the cross-range PSR as a function of the error $\epsilon(y)$. Note that (4) is the product of the ideal and error signals. For convenience, the phase error signal is denoted as $g(y) = \exp\{+j2k_0\epsilon(y)\}$ and the ideal signal history as $s(y) = \exp\{-j2k_0R(y)\}$. Taking the Fourier transform with respect to the spatial variable y causes

the transforms of these two functions to be related by convolution rather than multiplication. Thus, the PSR $f(y)$ due to any phase error $g(y)$ is given by the following expression:

$$\begin{aligned} f(y) &= \mathcal{F}_{k_y}^{-1}\{F(k_y)\} \\ &= \mathcal{F}_{k_y}^{-1}\{[S(k_y) *_{k_y} G(k_y)]\overline{S}(k_y)\}. \end{aligned} \tag{5}$$

The spectrum of the ideal signal phase history $S(k_y)$ is first convolved $(*_{k_y})$ with the spectrum of the error function $G(k_y)$, after which it is multiplied by $\overline{S}(k_y)$, the conjugate of the ideal signal history spectrum, to effect the correlation operation representing cross-range signal compression (1). An inverse Fourier transform in k_y yields the corrupted PSR. If $\epsilon(y) = 0$, then the ideal PSR is obtained and is given by $f_{\text{ideal}}(y) = \mathcal{F}_{k_y}^{-1}\left\{S(k_y)\overline{S}(k_y)\right\}$.

IV. Phase Error Analysis

This section presents several canonical examples of synthetic aperture phase errors. The linear, quadratic, and cubic terms may be used to represent more general low-frequency phase errors via truncated Taylor series [1]. The sinusoidal case is presented because it is encountered in practice and it can be used to synthesize more complicated phase error functions. Random white noise phase errors may occur as a result of electronic hardware noise, medium fluctuations, or errors in the motion estimation/compensation. Another case presented is that of a phase error represented by the sawtooth function. This case is common in SAS imaging, as it arises when the hydrophone array experiences a static yaw relative to the nominal platform trajectory. This usually occurs when the vehicle carrying the SAS encounters a cross current and attempts to maintain the desired path over the seafloor by adjusting its heading to point into the direction of current flow.

Polynomial errors higher than the cubic are not considered. According to Carrara *et al.* [1], the quartic and higher order terms fall into the same category as sinusoids with multiple cycles per synthetic aperture: That is, they are high-frequency errors, and the purpose of the Taylor series analysis is to examine low-frequency phase error functions. Low-frequency phase errors tend to primarily distort the mainlobe of the PSR, while high-frequency errors affect the sidelobe structure. The nature of the PSR distortion can take several forms, as is shown in the following.

A. Linear Phase Error

First, consider the specific example of a linear (or ramp) phase error: $\epsilon(y) = \alpha y$ and $g(y) = \exp\{j2k_0\alpha y\}$, where α is a dimensionless scale factor. The Fourier transform of this function is $G(k_y) = \delta(k_y - 2k_0\alpha)$. From (5), the effect in the k_y domain of a linear phase error is thus seen to be a shift of the ideal observed signal spectrum. Roughly speaking, the resolution of the PSR $f(y)$ is determined by the spatial bandwidth of the region of support common to $[S(k_y) *_{k_y} G(k_y)]$ and $\overline{S}(k_y)$[2], [6]. The detailed structural appearance of $f(y)$ will also be determined by the phase of $F(k_y)$. It is next shown that the loss of resolution, or PSR spread, is negligible for small values of α.

A closed-form expression for the distorted PSR can be obtained when the slope α of the linear phase error is small. The Fourier transform of the cross-range signal is

$$\begin{aligned} S(k_y) &= \sqrt{\frac{\pi x_0}{jk_0}}\text{rect}\left\{\frac{k_y}{\sin\theta_{3\text{dB}}\sqrt{4k_0^2 + k_y^2}}\right\} \\ &\quad \times \exp\left\{-j\left(\sqrt{4k_0^2 - k_y^2}\right)x_0\right\} \\ &\approx \sqrt{\frac{\pi x_0}{jk_0}}\text{rect}\left\{\frac{k_y}{4k_0\sin\frac{\theta_{3\text{dB}}}{2}}\right\} \\ &\quad \times \exp\left\{-j2k_0x_0 + j\frac{k_y^2}{4k_0}x_0\right\} \end{aligned} \tag{6}$$

where $\theta_{3\text{dB}}$ is the -3-dB beamwidth of the sensor (i.e., a single element of the physical SAS array), and the rectangle function is defined as $\text{rect}(x) = 1$ for $|x| \le 1/2$ and $\text{rect}(x) = 0$, otherwise. The first expression for $S(k_y)$ was derived [17] using the principle of stationary phase (PSP) [16], [18], [19]. The approximate expression for $S(k_y)$ was obtained by making a parabolic approximation to R in (1) and using the PSP to take the Fourier transform. The quadratic approximation to $S(k_y)$ is used below to facilitate the present analysis. It can be substituted into (5) to obtain the following:

$$\begin{aligned} f(y) &= \mathcal{F}_{k_y}^{-1}\left\{\left[A(k_y)\exp\left\{j\frac{k_y^2}{4k_0}x_0\right\} *_{k_y} \delta(k_y - 2k_0\alpha)\right]\right. \\ &\qquad \left.\times\, \overline{A}(k_y)\exp\left\{-j\frac{k_y^2}{4k_0}x_0\right\}\right\} \\ &= \mathcal{F}_{k_y}^{-1}\left\{A(k_y - 2k_0\alpha)\exp\left\{j\frac{(k_y - 2k_0\alpha)^2}{4k_0}x_0\right\}\right. \\ &\qquad \left.\times\, \overline{A}(k_y)\exp\left\{-j\frac{k_y^2}{4k_0}x_0\right\}\right\} \\ &= \mathcal{F}_{k_y}^{-1}\left\{A(k_y - 2k_0\alpha)\overline{A}(k_y)\exp\left\{j\left(k_0\alpha^2 - k_y\alpha\right)x_0\right\}\right\} \\ &\approx \mathcal{F}_{k_y}^{-1}\left\{|A(k_y)|^2\exp\left\{-jk_y\alpha x_0\right\}\right\} \\ &= f(y) *_y \delta(y - \alpha x_0) \\ &= f\left(y - \alpha x_0\right) \end{aligned} \tag{7}$$

where the term $A(k_y)$ represents the spectral amplitude combined with the complex constant $\exp\{-j2k_0x_0\}$ appearing in the last line of (6). The approximation step above was made by neglecting α in the amplitude term and α^2 in the phase term. The consequence of this approximation is that the effect of a linear phase error is to shift the k_y spectrum of the received signal. If this shift is small $(\alpha < 1)$, then the result of this spectral shifting is simply a shift in the cross-range position of the ideal PSR with negligible resolution loss. Fornaro *et al.* [6] reach the same conclusion.

The central result of this section is that spectral shifts of $2k_0\alpha$ translate into spatial shifts of αx_0 of the PSR. In other words, the convolutional relationship between $S(k_y)$ and $G(k_y)$ translates approximately into a convolutional relationship between $f(y)$ and a scaled/shifted version of $G(k_y)$. [See the first line of (7) compared to the second to last line.] This fact is used repeatedly below to derive closed-form estimates of PSR deterioration, and

it is the reason for the similarity between spotlight and stripmap image degradation due to unwanted phase errors.

B. Quadratic Phase Error

The quadratic phase error is generally considered to be the dominant cause of cross-range blur, or defocus, in synthetic aperture imagery. Apart from representing the second-order component of the Taylor series expansion of a given motion, the quadratic phase error can be used to model the effect of measurement errors in the wave propagation speed used for image reconstruction. As such, the analysis of quadratic error is also linked to the notion of depth of focus.

The quadratic phase error term is given by $g(y) = \exp\{j2k_0\nu y^2\}$ where ν is a scale factor having units of reciprocal length. Its Fourier transform obtained using the PSP is

$$G(k_y) = \sqrt{\frac{j\pi}{2k_0\nu}}\text{rect}\left(\frac{k_y}{4k_0\nu L_{\text{SA}}}\right)\exp\left\{-\frac{jk_y^2}{8k_0\nu}\right\}. \quad (8)$$

The error $g(y)$ has support on $y \in [-L_{\text{SA}}/2, L_{\text{SA}}/2]$. The exact and approximate quadratic phase error spectra $G(k_y)$ are shown in Fig. 1(a)

Using the reasoning upon which (7) is based, the degradation of the PSR can be estimated if it is assumed that the width of the rectangle function appearing in (8) is small. Then, the actual PSR can be thought of as a continuous smear of copies of the ideal PSR. The width of the actual PSR is determined by the width of the rectangle function in (8). Consequently, the fundamental type of degradation caused by the quadratic phase error is a broadening of the mainlobe relative to that of the ideal PSR. In other words, the quadratic phase error causes a loss of cross-range resolution. The expansion of the -3-dB width of the PSR can be estimated by the bandwidth of the rectangle function in (8) using the result of the approximation in (7). This expansion is found to be equal to $\Delta_{\text{PSR}} = 2\nu L_{\text{SA}} x_0 = 2\nu x_0^2 \sin\theta_{3\text{dB}}$. For a given value of ν, it is clear that the PSR width is proportional to the square of range. An example of the PSR degradation caused by the quadratic phase error is shown in Fig. 1(b).

It can now be shown that the effect of an error in the knowledge of the wave propagation speed can be modeled as a quadratic phase error. First, let the received signal be given by

$$\begin{aligned}\exp\{-j2(k_0+\Delta k)R\} &= \exp\{-j2k_0R\}\exp\{-j2\Delta kR\}\\ &= s(y)g(y)\end{aligned} \quad (9)$$

where the parabolic approximation to the phase term has replaced its true hyperbolic form $\left(R \approx x_0 + ((y^2)/(2x_0))\right)$ and the sound-speed error has been represented by a change in the temporal wave number $\Delta k = -(\omega\Delta c)/(c(c+\Delta c))$. The phase error function $g(y)$ has a form that is identical to the cross-range signal $s(y)$, and (6) may, therefore, be used to obtain $G(k_y)$ simply by substituting Δk for k_0. Consequently, the region of support for $G(k_y)$ is $\{k_y : |k_y| \le 2\Delta k \sin\theta_{3\text{dB}}/2 \approx \Delta k \sin\theta_{3\text{dB}}\}$, and the spread of the PSR corrupted by the sound-speed error is

$$\begin{aligned}\Delta_{\text{PSR}} &= \left|\frac{\Delta k}{k_0}\right| x_0 \sin\theta_{3\text{dB}}\\ &= \left|\frac{\Delta c}{c+\Delta c}\right| L_{\text{SA}}.\end{aligned} \quad (10)$$

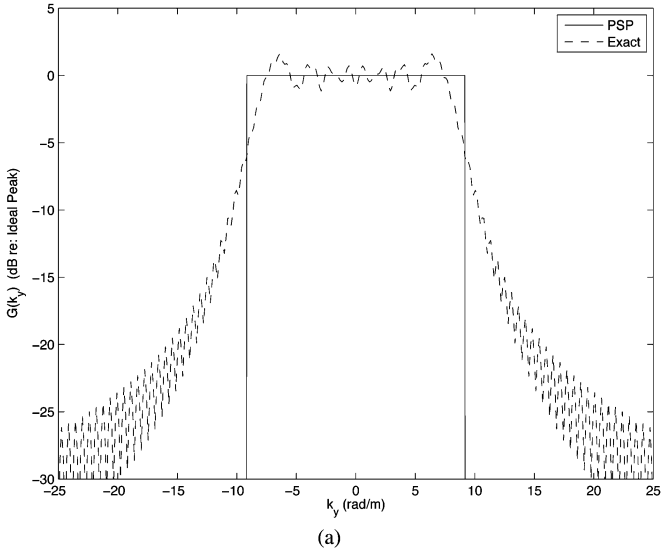

(a)

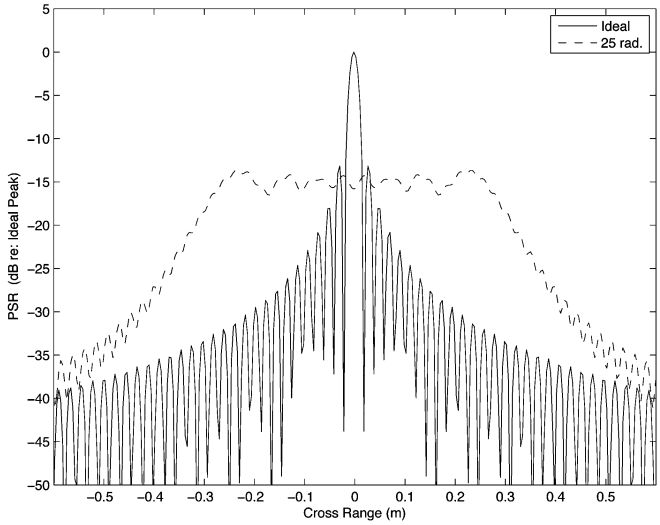

(b)

Fig. 1. (a) Comparison of the quadratic phase error spectrum $G(k_y)$ and the approximation given by (8), which was derived using the PSP. (b) Example of an ideal PSR and the PSR corrupted by a quadratic phase error. In both plots, the maximum quadratic phase error was 25 rad.

This corresponds to $\nu = \Delta c/(2x_0(c+\Delta c))$ in the result above. The error Δc causes the PSR degradation to become linearly proportional to the range.

Another useful application for this analysis is quantifying the effects of errors in the estimate of the sensor's forward (i.e., cross-range) velocity. For this situation, the cross-range location of the sensor is (wrongly) believed to be at $y + \chi y$ when it is in fact located at y. The quantity χ represents the fractional error in the velocity estimate. That is, $\chi = (v_{\text{est}} - v_{\text{act}})/v_{\text{act}}$. Then, the range becomes $R = \sqrt{x_0^2 + (y+\chi y)^2}$ which is approximated, for $\chi \ll 1$, as $R \approx x_0 + (1+2\chi)y^2/2x_0$ and the phase error function is given by

$$g(y) = \exp\left\{-\frac{j2k_0\chi y^2}{x_0}\right\}. \quad (11)$$

The corresponding Fourier transform is

$$G(k_y) = \sqrt{\frac{\pi x_0}{j2k_0\chi}}\mathrm{rect}\left\{\frac{x_0 k_y}{4k_0\chi L_{\mathrm{SA}}}\right\}\exp\left\{-j\frac{3x_0k_y^2}{8k_0\chi}\right\} \tag{12}$$

from which the corrupting PSR spread is found to be $\Delta_{\mathrm{PSR}} = 2|\chi|L_{\mathrm{SA}}$. According to [20], the results of this and the preceding paragraph can be obtained in an alternative manner using the principles of geometrical optics.

C. Cubic Phase Error

While the quadratic phase error degrades the PSR symmetrically, the cubic phase error term does so in an asymmetric fashion. Both errors decrease the resolution (-3-dB width of the PSR). The PSP is once again used to facilitate the analysis, as it is necessary to know the Fourier transform of $g(y) = \exp\{j2k_0\rho y^3\}$, where ρ is a constant with dimension of length^{-2}

$$G(k_y) = \int_{-L/2}^{L/2} e^{j2k_0\rho y^3}e^{-jk_y y}dy. \tag{13}$$

The stationary point of (13) is

$$y^{\diamond} = \pm\sqrt{\frac{k_y}{6k_0\rho}} \tag{14}$$

and the question arises as to which sign is the correct one to take for the present application. Substituting $y^{\diamond}$ into the PSP phase term $\exp\{j\phi(y^{\diamond})\}$ gives

$$\exp\{j\phi(y^{\diamond})\} = \exp\left\{\mp j\frac{2k_y}{3}\sqrt{\frac{k_y}{6k_0\rho}}\right\}. \tag{15}$$

If the signs of k_y and the constant ρ differ, then the argument of this exponential becomes purely real. Thus, one finds motivation for choosing the positive sign in (14) to avoid exponential growth in $G(k_y)$. The next term to examine in the PSP analysis is the envelope term. As usual, the envelope of $g(y)$ is a rectangle function centered at $y = 0$ and having width L_{SA}. This leads to the following for the envelope of $G(k_y)$:

$$\begin{aligned} g_0(y^{\diamond}) &= \mathrm{rect}\left(\frac{y^{\diamond}}{L_{\mathrm{SA}}}\right) \\ &= \mathrm{rect}\left(\sqrt{\frac{k_y}{6k_0\rho L_{\mathrm{SA}}^2}}\right). \end{aligned} \tag{16}$$

In this equation, it must be recognized that the argument of the rectangle function can become complex. To deal with this situation, the definition of this function is extended such that $\mathrm{rect}(x)$ equals one if x is both real and $|x| \le 1/2$. For all other values of x, $\mathrm{rect}(x) = 0$. Therefore, (16) indicates that the PSP approximation to the spectrum $G(k_y)$ is one-sided. It is given by

$$G(k_y) \approx \frac{\sqrt{j\pi}}{(6\rho k_0 k_y)^{1/4}}\mathrm{rect}\left(\sqrt{\frac{k_y}{6k_0\rho L_{\mathrm{SA}}^2}}\right)\exp\left\{j\sqrt{\frac{k_y}{6k_0\rho}}\right\}. \tag{17}$$

The region of spectral support of $G(k_y)$ for the cubic phase error function is $\{k_y : 0 \le k_y \le 3k_0\rho L_{\mathrm{SA}}^2/2\}$ if $\rho > 0$. If ρ is negative, then $G(k_y)$ has support given by $\{k_y : 3k_0\rho L_{\mathrm{SA}}^2/2 \le k_y \le 0\}$. Applying the reasoning from (7) as before, the expansion of the PSR due to the cubic phase error function is $\Delta_{\mathrm{PSR}} = 3\rho L_{\mathrm{SA}}^2 x_0/4$. The stationary phase approximation to $G(k_y)$ is compared to the actual spectrum in Fig. 2(a). The resulting PSR is shown in Fig. 2(b). Unlike the quadratic case, the spread given by Δ_{PSR} does not fully describe the appearance of the PSR corrupted by a cubic phase error. Here, the PSR sidelobe structure tapers off gradually from the peak mainlobe value before finally reaching the "knee" or cutoff predicted by Δ_{PSR}, at which point the sidelobe magnitude falls off more rapidly.

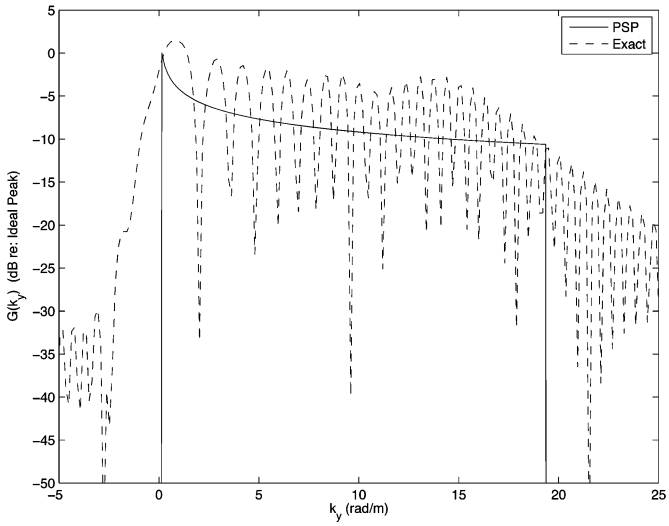

(a)

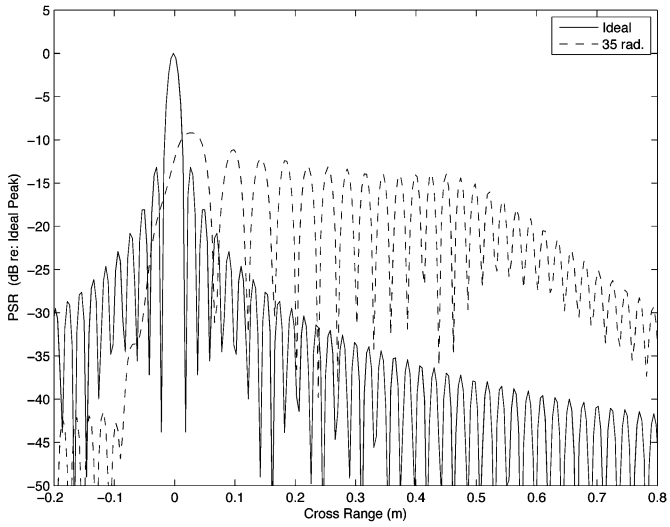

(b)

Fig. 2. (a) Comparison of the cubic phase error spectrum $G(k_y)$ and the approximation given by (17), which was derived using the principle of stationary phase. (b) Example of an ideal PSR and the PSR corrupted by a cubic phase error. In both plots, the maximum phase error was 35 rad.

D. Sinusoidal Phase Error

Another interesting case is that of a sinusoidal phase error $g(y) = \exp\{j2k_0\beta\sin(\gamma y)\}$. The constant β has dimension of

length, and γ has dimension of reciprocal length. The analysis of this section is largely based on the work by Fornaro [5]. The function $g(y)$ can be manipulated into a more useful form by employing the generating function for the Bessel function of the first kind

$$\exp\left\{\frac{x}{2}\left(t-\frac{1}{t}\right)\right\}=\sum_{n=-\infty}^{\infty}t^n J_n(x) \tag{18}$$

and making the substitutions $t=\exp\{j\gamma y\}$ and $x=2k_0\beta$. The result is

$$\exp\left\{j2k_0\beta\sin(\gamma y)\right\}=\sum_{n=-\infty}^{\infty}\left(e^{j\gamma y}\right)^n J_n(2k_0\beta). \tag{19}$$

Taking the Fourier transform of this with respect to y gives $G(k_y)$

$$G(k_y)=\sum_{n=-\infty}^{\infty}J_n(2k_0\beta)\delta\left(k_y-n\gamma\right). \tag{20}$$

Thus, a sinusoidal phase error will result in the creation of replicas of the ideal observed signal spectrum $S(k_y)$. These replicas are weighted according to the value of the coefficient $J_n(2k\beta)$. Although there is an infinite number of replicas, the coefficients die off quickly. The rate of decay slows with increasing sinusoidal amplitude β, and the replica spacing is determined by the frequency γ of the phase error function. Fig. 3(a) shows $G(k_y)$ for a representative value of $k_0\beta$ and B_{k_y}/γ. These quantities are dimensionless and represent the relative error magnitude compared to the wavelength and the error frequency relative to the spatial frequency bandwidth observable by the synthetic aperture, respectively. (Recall that $B_{k_y}=4k_0\sin(\theta_{3\text{dB}}/2)\approx 2k_0\sin\theta_{3\text{dB}}\approx 4\pi/D$.) Assuming β and γ are within certain bounds, then the result from Section IV-A may be used to deduce that a sinusoidal phase error results in multiple scaled copies of the ideal PSR

$$f_{\text{composite}}=\sum_{n=-\infty}^{\infty}J_n(2k_0\beta)f\left(y-\frac{n\gamma}{2k_0}x_0\right). \tag{21}$$

These replicas are located at $y=\pm n\gamma x_0/2k_0$. Note that the scale factor $J_n(2k_0\beta)$ depends on k_0. Fig. 3(b) shows an example of these results. A similar result is derived in [1], but only the terms for $n=-1,0$, and $+1$ in (19) are retained.

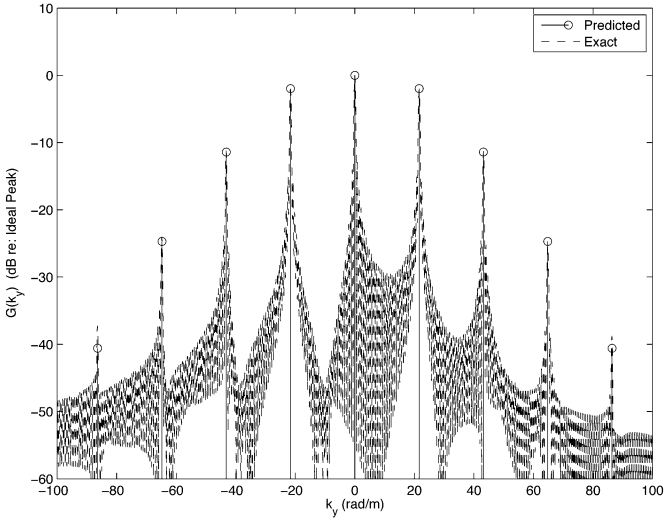

(a)

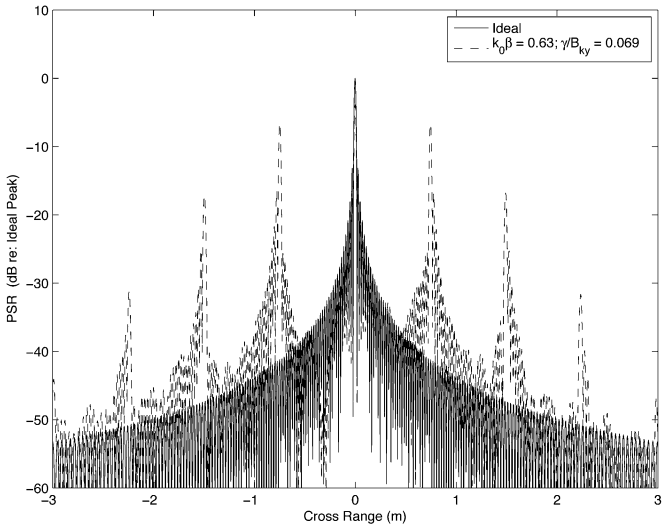

(b)

Fig. 3. (a) Comparison of the actual sinusoidal phase error spectrum $G(k_y)$ and the closed-form expression given by (20). The actual (or experimental) $G(k_y)$ was computed discretely, and it, therefore, does not consist of delta functions as does the ideal result. (b) Example of an ideal PSR and the PSR corrupted by a sinusoidal phase error. In both plots, the parameters used were $k_0\beta=0.63$ and $\gamma/B_{k_y}=0.069$.

E. Sawtooth Phase Error

The preceding analysis can be used to derive the effect of a sawtooth-shaped phase error $g(y)=\exp\{j2k_0\xi(y)\}$, where $\xi(y)$ is the sawtooth function with period P and peak-to-peak amplitude A. This case is important because it is frequently (if not universally) encountered in practice. It is common for towed and autonomous SAS sensors to travel in some degree of cross current. In these situations, the host platform usually experiences a static yaw to keep the desired course over the bottom. This fact is the motivation for the forward fins that were developed for the REMUS600 vehicle chosen to carry the Small Synthetic Aperture Minehunter (SSAM) sonar developed by the U.S. Office of Naval Research (Arlington, VA) [21].

A single-projector, multiple-receiver configuration is known as a vernier array and is almost always used for SAS because it increases the area coverage rate. The combination of static yaw and a vernier SAS array leads to a sawtooth phase error superimposed on the observed SAS signals. The peak-to-peak amplitude of this error is $A=ND\sin(\theta_{\text{crab}})/2\approx ND\theta_{\text{crab}}/2$, where N is the number of receivers of length D and θ_{crab} is the static yaw angle. The period of the sawtooth pattern is, of course, $P=ND\cos(\theta_{\text{crab}})/2\approx ND/2$. In general, the static yaw (or crab) angle is fairly small, and the approximations given are sufficiently accurate. The Fourier series representation of the sawtooth wave is

$$\begin{aligned}\xi(y)&\approx\frac{A}{\pi}\left(\sin\frac{2\pi y}{P}-\frac{1}{2}\sin\frac{4\pi y}{P}+\frac{1}{3}\sin\frac{6\pi y}{P}-\cdots\right)\\&=\frac{A}{\pi}\sum_{m=1}^{\infty}\frac{(-1)^{m-1}}{m}\sin\frac{2m\pi y}{P}\\&=\frac{ND\theta_{\text{crab}}}{2\pi}\sum_{m=1}^{\infty}\frac{-1^{m-1}}{m}\sin\frac{4m\pi y}{ND}.\end{aligned} \tag{22}$$

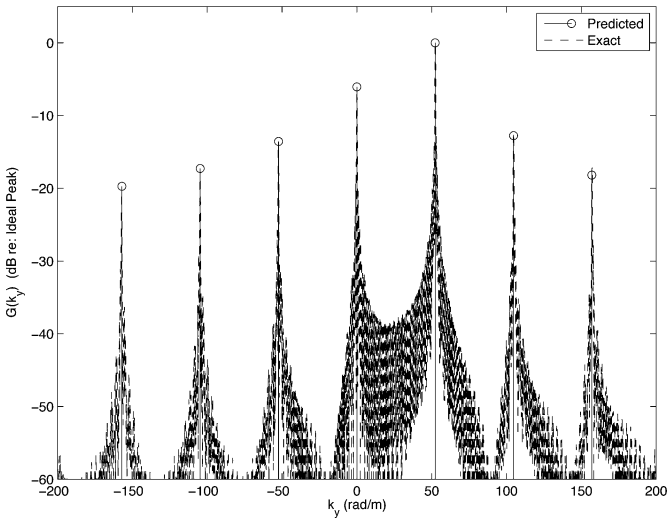

(a)

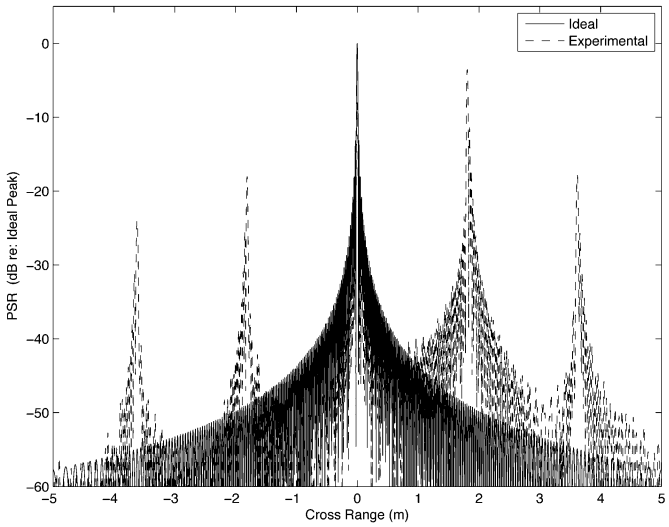

(b)

Fig. 4. (a) Comparison of the actual sawtooth phase error spectrum $G(k_y)$ and the expression given by (23). The actual (or experimental) $G(k_y)$ was computed discretely, and it, therefore, does not consist of delta functions as does the ideal result. For this example, the parameters are $D = 0.4$, $\theta_{\text{crab}} = 2^\circ$, and $N = 6$. (b) Example of an ideal PSR and the PSR corrupted by a sawtooth phase error with the same parameters given in Fig. 4(a).

This infinite sum appears in the exponential term of $g(y)$, and $g(y)$ can, therefore, be written as an infinite series of products. Recall from the previous section that the Fourier transform of any single term in this product is an infinite sum in the k_y domain. For the sawtooth case, $G(k_y)$ is an infinite series of convolutions of infinite sums

$$\begin{aligned} G(k_y) &= \mathcal{F}_y\{g(y)\} \\ &= \mathcal{F}_y\left\{\prod_{m=1}^{\infty}\exp\left\{j2k_0\frac{A(-1)^{m-1}}{m\pi}\sin\frac{2m\pi y}{P}\right\}\right\} \\ &= G_1(k_y) *_{k_y} G_2(k_y) *_{k_y} G_3(k_y)\ldots \end{aligned} \tag{23}$$

where each of the $G_m(k_y)$ in the last line of (23) is the Fourier transform of a single component of (22) and has the form of (20). An example is shown in Fig. 4(a). Unfortunately, there is no convenient closed-form expression for the corrupted PSR due to the sawtooth phase error. It is true that the replicas due to any single sinusoidal component generally decay quickly. The same is not true for the amplitudes of the terms of the Fourier series $\xi(y)$ because of the discontinuity present in the sawtooth function.

The characteristic feature of the sawtooth phase error is that the infinite series of convolutions is such that the replicas of the PSR are not symmetrically weighted. As one would expect, the sawtooth error causes a dominant replica to occur either to the left or to the right of the real object depending on whether the array is squinted fore or aft. The distance between the replicas induced by the phase error is

$$y = \frac{2\pi}{NDk_0}x_0. \tag{24}$$

Fig. 4(b) shows how the replicas of the PSR are evenly spaced but unevenly weighted. It is also important to point out that it is possible for one of the replicas of the PSR to have an amplitude greater than the "true" PSR located at $y = 0$. Last, it should be noted that this analysis ignores the amplitude weighting effect associated with the beam patterns of the crabbed physical array.

F. Normally Distributed Random Phase Error

The final case to be considered is a random phase error: $g(y) = \exp\{j\kappa(y)\}$, in which $\kappa(y)$ is a normally distributed zero-mean white random process with variance σ_κ^2. Because the process $\kappa(y)$ is stationary, the expected value is independent of y. Consequently, it is expressed as

$$\begin{aligned} E\{e^{j\kappa}\} &= \mu_g \\ &= E\{\cos(\kappa)\} + jE\{\sin(\kappa)\} \\ &= \int_{-\infty}^{\infty}\cos(\kappa)\frac{e^{-\kappa^2/2\sigma_\kappa^2}}{\sqrt{2\pi\sigma_\kappa^2}}d\kappa \\ &\quad + j\int_{-\infty}^{\infty}\sin(\kappa)\frac{e^{-\kappa^2/2\sigma_\kappa^2}}{\sqrt{2\pi\sigma_\kappa^2}}d\kappa. \end{aligned} \tag{25}$$

A closed-form expression for this expected value was derived by Richards [22] who obtained $\mu_g = \exp\{-\sigma_\kappa^2/2\}$. Fig. 5 shows the result of carrying out the integration in (25) numerically for values of σ_κ^2 ranging from 0.01 to 100. The plot shows the expected value for the real and imaginary parts separately. The expected value of the complex part of the random process is always zero, agreeing with the result in [22].

For small variance in the phase noise, the value of (25) is close to one. As the variance becomes large, the expected value approaches zero. This makes intuitive sense because the phase error function $g(y)$ effectively becomes a vector of unit length whose angle in the complex plane is uniformly distributed. Note that the quotient σ_κ/k_0 can be used to express the variance in terms of dimension of length. Similarly, the standard deviation in terms of wavelengths is $\sigma_\kappa/2\pi$. Also of interest is the variance of $g(y)$

$$\begin{aligned} \text{var}\{g(y)\} &= E\{|g(y) - \mu_g|^2\} \\ &= E\{|e^{j\kappa(y)} - \mu_g|^2\} \\ &= E\{|e^{j2\kappa(y)}|^2\} - |\mu_g|^2 \\ &= 1 - \mu_g^2. \end{aligned} \tag{26}$$

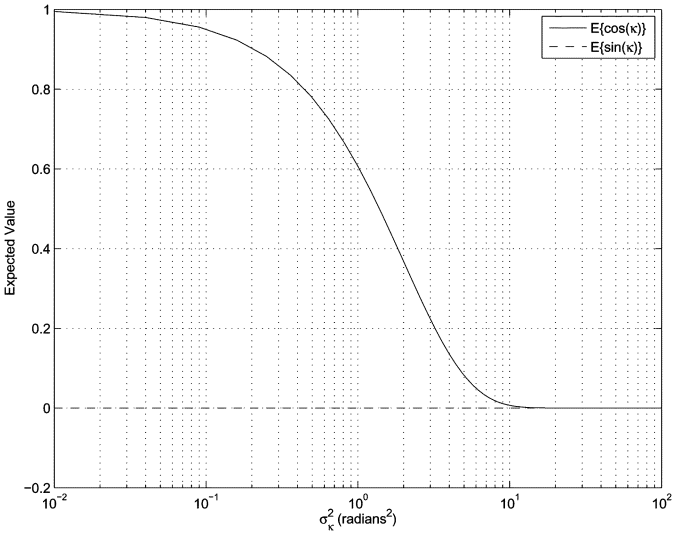

Fig. 5. Expected value of the real and imaginary components of (25) evaluated for values of σ_κ^2 ranging from 0.01 to 100.

Interestingly, the variance of $g(y)$ can be expressed solely in terms of its expected value.

The effect of the random phase error can be summarized by the expected value of the magnitude of the PSR $E(|f(y)|^2)$. This quantity is obtained using the following facts regarding linear systems with random processes as inputs [23, p. 237]:

$$R_{pq}(t_1,t_2) = \int_{-\infty}^{\infty} R_{pp}(t_1, t_2-\alpha)\overline{h}(\alpha)d\alpha \tag{27}$$

$$R_{qq}(t_1,t_2) = \int_{-\infty}^{\infty} R_{pq}(t_1-\alpha, t_2)h(\alpha)d\alpha \tag{28}$$

where R represents the correlation of the subscripted signals, $h(t)$ represents the system impulse response, $p(t)$ is its input, and $q(t)$ is its output. The result above enables one to find the autocorrelation of the output using only the autocorrelation of the input and the system impulse response. The quantity of ultimate interest is the expected value of the squared magnitude of the corrupted PSR $E(|f(y)|^2)$; this is equal to the autocorrelation of $f(y)$ evaluated for zero lag.

In the following analysis, the corrupted received signal $s_c(y) = s(y)g(y)$ is taken as the input $p(t)$ while $\overline{s}(y)$ plays the role of the linear system impulse response $h(t)$. The output $q(t)$ above corresponds to the PSR $f(y)$. Recall that the ideal PSR can be thought of as the autocorrelation of $s(y)$, $R_{ss}(y')$ (i.e., $h = 1$). The first step is to find the autocorrelation of $s_c(y)$ employing the fact that $g(y)$ can be expressed as the sum of its mean and the centered version of itself $g(y) = \mu_g + (g(y) - \mu_g) = \mu_g + \nu(y)$

$$\begin{aligned}
&R_{s_cs_c}(y_1,y_2)\\
&\quad= E\{s_c(y_1)\overline{s_c}(y_2)\}\\
&\quad= E\{s(y_1)g(y_1)\overline{s}(y_2)\overline{g}(y_2)\}\\
&\quad= E\{[\mu_g s(y_1)+\nu(y_1)s(y_1)][\mu_g\overline{s}(y_2)+\overline{\nu}(y_2)\overline{s}(y_2)]\}\\
&\quad= \mu_g^2 s(y_1)\overline{s}(y_2) + E\{\nu(y_1)s(y_1)\overline{\nu}(y_2)\overline{s}(y_2)\}\\
&\quad= \mu_g^2 s(y_1)\overline{s}(y_2) + \sigma_g^2\delta(y_2-y_1).
\end{aligned} \tag{29}$$

Note that $s(y)$ disappears in the last term of the final line of (29) because of the action of the delta function and the fact that $s(y)\overline{s}(y)$ is equal to one. The next step is to compute R_{s_cf}

$$\begin{aligned}
R_{s_cf}(y_1,y_2) &= R_{s_cs_c}(y_1,y_2) *_{y_2} s(y_2)\\
&= \left[\mu_g^2 s(y_1)\overline{s}(y_2) + \sigma_g^2\delta(y_2-y_1)\right] \odot_{y_2} s(y_2)\\
&= \mu_g^2 s(y_1)\overline{f}(y_2) + \sigma_g^2 s(y_2-y_1),
\end{aligned} \tag{30}$$

followed by R_{ff}

$$\begin{aligned}
R_{ff}(y_1,y_2) &= R_{s_cf}(y_1,y_2) *_{y_1} \overline{s}(y_1)\\
&= \left[\mu_g^2 s(y_1)\overline{f}(y_2) + \sigma_g^2 s(y_2-y_1)\right] \odot_{y_1} \overline{s}(y_1)\\
&= \mu_g^2 f(y_1)\overline{f}(y_2) + \sigma_g^2 f(y_2-y_1).
\end{aligned} \tag{31}$$

Finally, if $y_2 = y_1 = y$, the desired result is obtained

$$R_{ff}(y,y) = E\{|f(y)|^2\} = \mu_g^2|f(y)|^2 + \sigma_g^2 f(0). \tag{32}$$

Note that $f(0)$ is real and is equal to L_{SA}

$$f(0) = \int_{-L_{\mathrm{SA}}/2}^{L_{\mathrm{SA}}/2} s(y)\overline{s}(y)dy.$$

It is now possible to quantify the effect of a normally distributed white random phase on the ideal PSR. It can be seen that the corrupted PSR consists of a copy of the ideal PSR scaled by μ_g^2 and added to a background value. As the variance of the phase noise increases, the scaled copy of the ideal PSR diminishes in amplitude relative to the mean background noise. The amplitude of the peak of the corrupted PSR relative to the ideal is given in decibels by

$$\begin{aligned}
\text{actual-to-ideal-peak ratio} &= 10\log_{10}\mu_g^2\\
&= 10\log_{10} e^{-\sigma_\kappa^2}.
\end{aligned} \tag{33}$$

Similarly, the actual peak relative to the background level is given by

$$\begin{aligned}
\text{actual-peak-to-mean-background ratio} &= 10\log_{10}\frac{\mu_g^2 L_{\mathrm{SA}}}{\sigma_g^2}\\
&= 10\log_{10}\frac{\mu_g^2 L_{\mathrm{SA}}}{1-\mu_g^2}\\
&= 10\log_{10}\frac{e^{-\sigma_\kappa^2}L_{\mathrm{SA}}}{1-e^{-\sigma_\kappa^2}}.
\end{aligned} \tag{34}$$

where L_{SA} is expressed in terms of normalized length, in accordance with the fact that any decibel scale requires a reference. Equation (34) confirms analytically what is well-known experientially: random phase errors result in an overall lack of image contrast but no loss of resolution. For a given noise variance, this effect diminishes with range as the synthetic aperture length grows. Fig. 6(a) gives an example of an actual PSR and the PSR

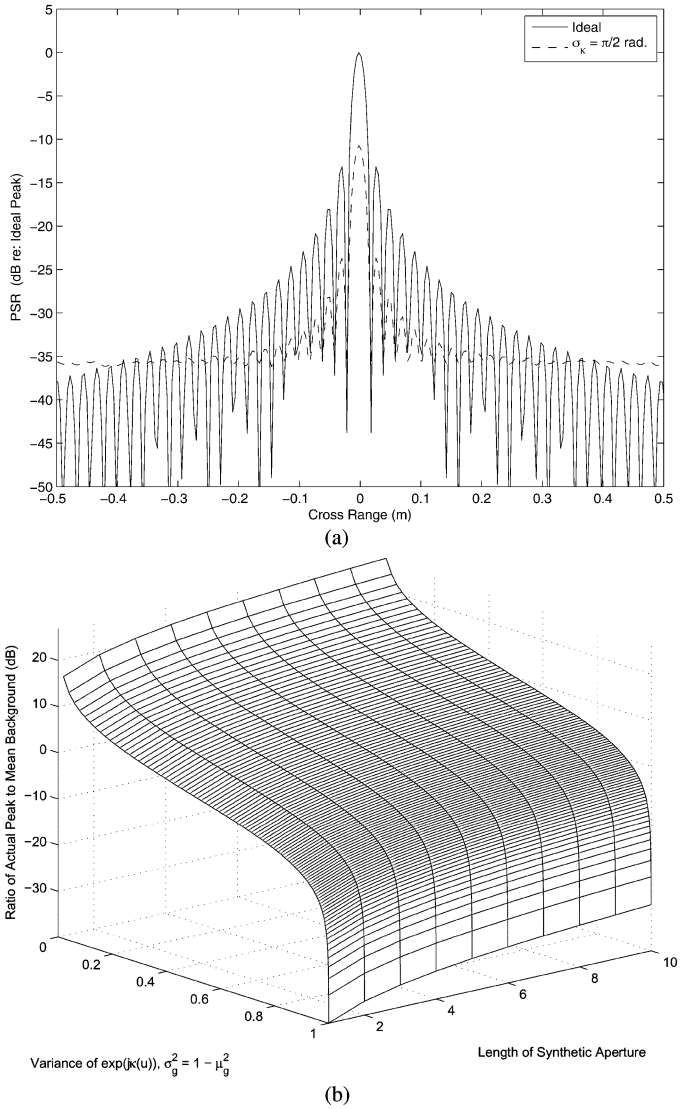

Fig. 6. (a) Example of an ideal PSR and the PSR corrupted by a normally distributed white random phase error whose standard deviation corresponds to one quarter of a wavelength. (b) Surface plot depicting the actual peak-to-background ratio (in decibels) as a function of μ_g and the synthetic aperture length. The quantity μ_g is unitless, while L_{SA} is expressed as normalized length (i.e., the actual length divided by the unit length in the given system of measurement).

subject to random phase noise with $\sigma_\kappa = 2\pi/4$ rad. One thousand realizations were averaged to compute the corrupted PSR. For this example, the theoretical value for the actual peak relative to the ideal is -10.9 dB and the value for the actual peak relative to the background is 28.3 dB. The plot indicates a value slightly less than 28.3 dB for the peak-to-background ratio. This apparent anomaly is because the horizontal extent of the PSR contained in the plot includes the sidelobe structure in addition to the background noise. For cross-range values well beyond ± 0.5 m, the peak-to-background ratio approaches the predicted 28.3 dB. Additionally, Fig. 6(b) depicts the behavior of (34) as a function of both μ_g and L_{SA}. The peak-to-background ratio improves as the synthetic aperture length grows. In practice, this means that narrowbeam and short-range SAS systems are the most susceptible to random phase errors of a given variance.

V. Discussion

The preceding results are applied to actual SAS field data in Fig. 7(a)–(f). This data was collected by the high-frequency band of the SSAM [21]. This sonar operates from 105 to 135 kHz with physical receiver elements that are 0.04 m wide.

The test image appearing in Fig. 7 was first motion compensated to obtain proper focus. Then, each of the errors analyzed in Section IV was applied to the data to yield the set of images shown. The $\omega - k$ algorithm was used to reconstruct the imagery, and rectangular spectral weighting was used to match the 1-D results in Section IV. The parameters used to produce Fig. 7 are the same as the counterpart examples in Section IV. The object shown is a tetrahedron approximately 2 m across. The forms of distortion visible in the images are in good agreement with those predicted above. Some 2-D distortion is visible because of the large magnitude of the phase errors used for the illustration. Such distortion in range is not discussed in this paper, and [7] asserts that range blurring effects due to phase/motion errors are generally an order of magnitude less significant than in the azimuth direction. Fig. 7 appears to justify this claim.

While the analytical results were derived for a single temporal frequency, the finite-bandwidth condition can be modeled by computing the degraded PSR for a range of temporal frequencies within a desired band and then summing the results. Fig. 8(a) and (b) shows two examples of such a computation assuming a center-frequency-to-bandwidth ratio of four, corresponding to the parameters used to create Fig. 7. The phase error function parameters are the same as those used to produce Figs. 3(b) and 4(b).

The results of Section IV are presented without any sort of spectral weighting or windowing. This was done to facilitate the derivation of closed-form expressions for the PSR behavior. Such weighting is, however, generally considered to be standard practice for controlling the sidelobe behavior of the PSR. Fig. 9 shows the result of Taylor weighting ($\bar{n} = 5$ with -35-dB sidelobes) applied to various amounts of quadratic phase error. The figure clearly shows that spectral apodization can go a long way toward blunting the deleterious effects of phase errors on the stripmap PSR.

It is the authors' experience that random phase noise observed in AUV-based SAS does not originate directly from vehicle motion. Nevertheless, the analysis from Section IV-F can be used to model at least two practical scenarios. First, it can be used to study the effects of timing errors in data acquisition hardware. Although this problem is easy to address in practice, it can be crippling if overlooked. Second, the random phase error can be used to model the effects of noise on the motion estimation/compensation procedure. One practical example occurs when external sensors are used for estimating the motion experienced by the SAS. SAS motion compensation is typically done using the redundant phase center (RPC) technique [also known as the displaced phase center antenna (DCPA) method], which uses the SAS data itself [24]. While the RPC approach is very good at estimating translations, it is less well suited for measuring rotations. Hence, SAS motion estimation algorithms are

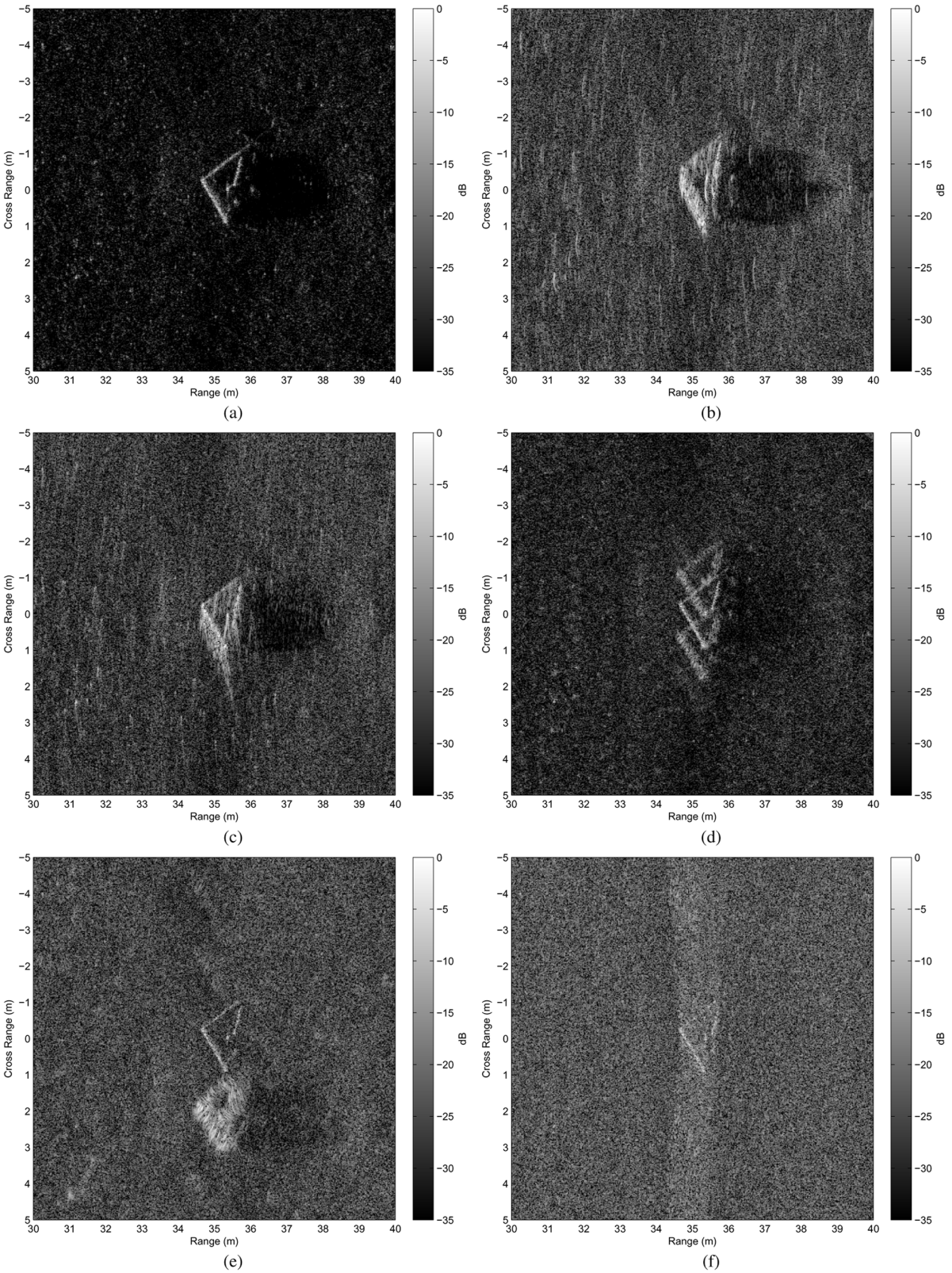

Fig. 7. Examples of the effects of the phase errors discussed in Section IV: (a) no error; (b) quadratic error; (c) cubic error; (d) sinusoidal error; (e) sawtooth error; and (f) random error. The parameters used are the same as for the figures appearing in Section IV.

frequently constructed around RPC aided by angular rate sensors. Electrical interference on these would be misinterpreted as high-frequency motion and would lead to degraded imagery. The noisy sensor data can be smoothed as a precaution, but then, low-frequency phase errors can arise if the smoothing is too aggressive.

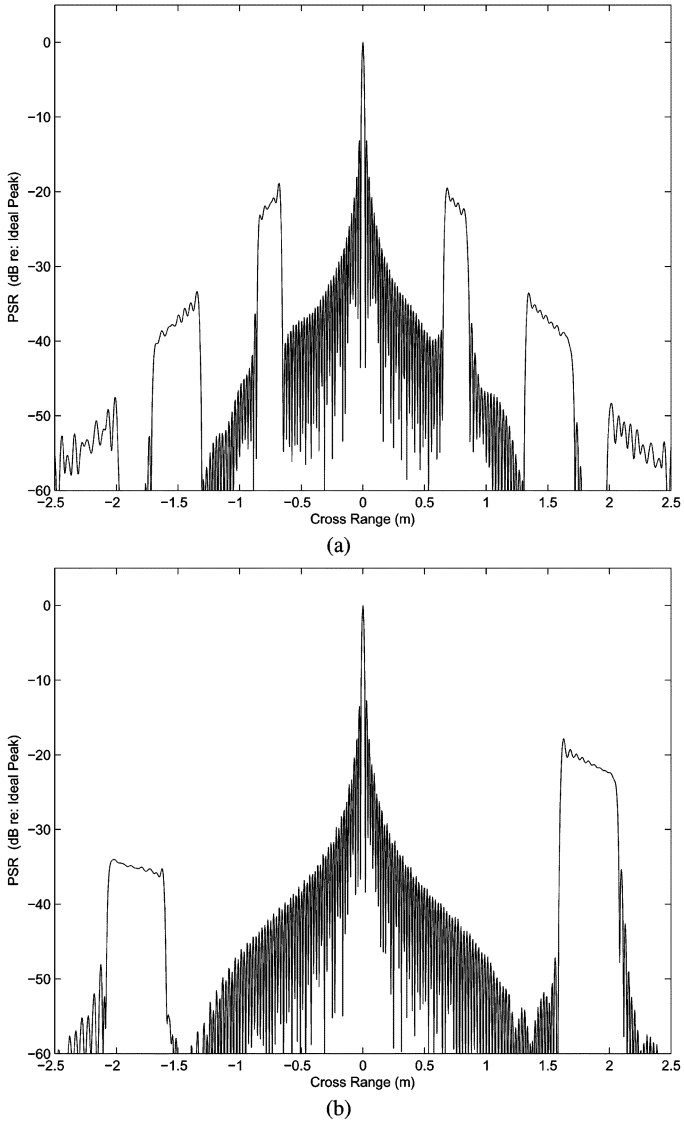

Fig. 8. Result of applying the single-frequency results of Section IV to a finite-bandwidth signal. This was achieved by summing the single-frequency PSRs over a range of frequencies. Shown are the (a) sinusoidal and (b) sawtooth phase errors for a signal with a center-frequency-to-bandwidth ratio of four, corresponding to the SSAM [21]. These plots are the finite-bandwidth equivalent of Figs. 3(b) and 4(b) where the ideal PSR is omitted and the horizontal axis is enlarged by a factor of two.

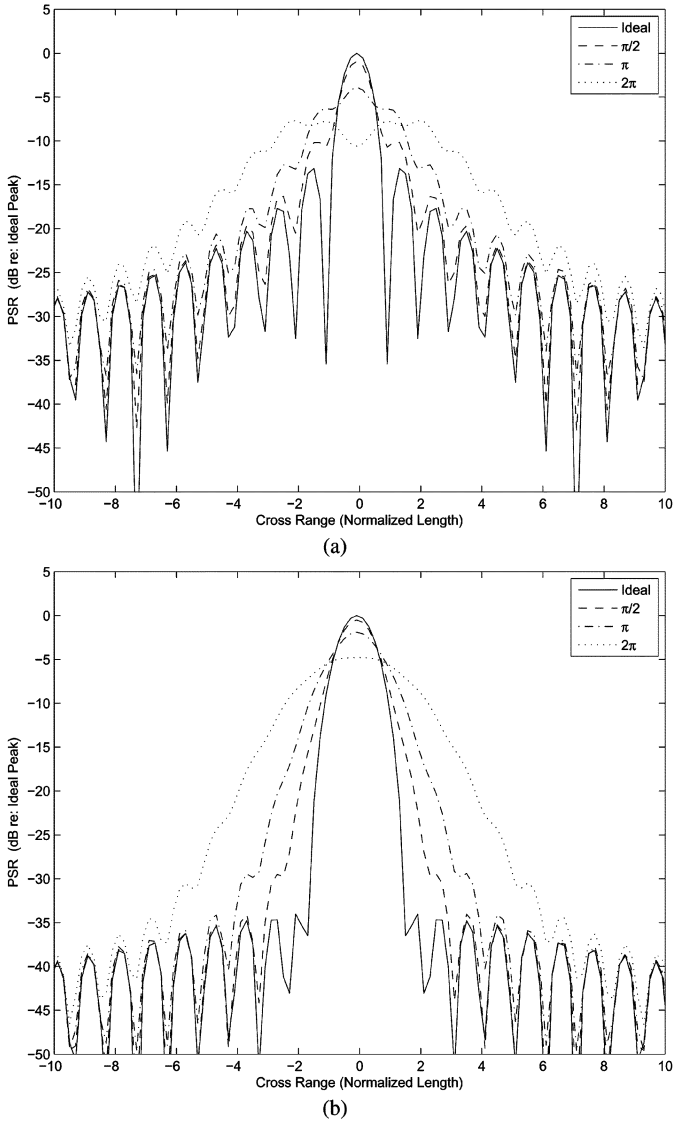

Fig. 9. Synthetic aperture PSR as influenced by various degrees of quadratic phase error: (a) rectangular weighting is applied; (b) created using a Taylor window with $\bar{n} = 5$ and -35-dB sidelobes. The horizontal axis is normalized length, where the interval $[-0.5, 0.5]$ corresponds to the ideal cross-range resolution $D/2$.

VI. Conclusion

The analysis began with the assumption of narrowbeam physical apertures and small (or residual) motion errors that are less than a resolution cell in extent. This simplification restricts the discussion to phase errors. A similar treatment for the linear and sinusoidal cases is given in the SAR literature by Fornaro *et al.* [5] in which no prior restrictions are placed on the magnitude of the motion errors. These authors then develop an exact expression for the 2-D spectrum of the observed synthetic aperture data. This spectral model is in turn simplified using the small-magnitude error assumption. Closed-form expressions for various types of phase errors can be obtained from this simplified model.

It was shown that the analysis of stripmap phase errors is different than for the spotlight mode. Nevertheless, the results are similar for the two imaging modalities. For example, sinusoidal errors generate replicas of the PSR while random high-frequency errors induce a loss of contrast without a loss of resolution. The overall taxonomy for describing the qualitative effects of phase errors on stripmap imaging is essentially the same as for spotlight imaging, as presented by Carrara *et al.* [1]. These results are useful in a variety of applications such as error budgeting for system design, developing improved strategies for data collection, and diagnosing the sources of image degradation for experimental data.

Acknowledgment

The authors would like to thank the U.S. Office of Naval Research for its long-standing sponsorship of SAS development. This commitment is being rewarded as the technology matures and proves itself to be a robust tool for observing the seafloor in

unprecedented detail. It is truly a privilege to have the opportunity to participate in this endeavor. The authors also would like to thank Dr. M. Richards of Georgia Institute of Technology for a number of enlightening discussions regarding SAR. Last, and on a personal note, the authors would like to express their sincere gratitude to J. Fernandez for his leadership, patient mentoring, and for sharing some of his encyclopedic knowledge of his field.

REFERENCES

[1] W. G. Carrara, R. S. Goodman, and R. M. Majewski, *Spotlight Synthetic Aperture Radar Signal Processing Algorithms*. Norwood, MA: Artech House, 1995.

[2] R. O. Harger, *Synthetic Aperture Radar Systems*. New York: Academic, 1970.

[3] W. M. Brown, "SAR resolution in the presence of phase errors," *IEEE Trans. Aerosp. Electron. Syst.*, vol. AES-24, no. 6, pp. 808–814, Nov. 1988.

[4] C. J. Oliver, "Synthetic aperture imaging algorithms," *J. Phys. D: Appl. Phys.*, vol. 22, pp. 871–890, 1989.

[5] G. Fornaro, "Trajectory deviations in airborne SAR: Analysis and compensation," *IEEE Trans. Aerosp. Electron. Syst.*, vol. 35, no. 3, pp. 997–1009, Jul. 1999.

[6] G. Fornaro, G. Franceschetti, and S. Perna, "Motion compensation errors: Effects on the accuracy of airborne SAR images," *IEEE Trans. Aerosp. Electron. Syst.*, vol. 41, no. 4, pp. 1338–1352, Oct. 2005.

[7] K. A. C. de Macedo and R. Scheiber, "Precise topography- and aperture-dependent motion compensation for airborne SAR," *IEEE Geosci. Remote Sens. Lett.*, vol. 2, no. 2, pp. 172–176, Apr. 2005.

[8] C. V. Jakowatz, D. E. Wahl, P. H. Eichel, D. C. Ghiglia, and P. A. Thompson, *Spotlight-Mode Synthetic Aperture Radar: A Signal Processing Approach*. Norwell, MA: Kluwer, 1996.

[9] D. C. Munson, Jr, J. D. O'Brien, and W. K. Jenkins, "A tomographic formulation of spotlight-mode synthetic aperture radar," *Proc. IEEE*, vol. 71, no. 8, pp. 917–925, Aug. 1983.

[10] M. A. Richards, *Fundamentals of Radar Signal Processing*. New York: McGraw-Hill, 2005.

[11] T. S. Durrani and D. Bisset, "The radon transform and its properties," *Geophysics*, vol. 49, no. 8, pp. 1180–1187, Aug. 1984.

[12] D. E. Wahl, C. V. Jakowatz, Jr, P. A. Thompson, and D. C. Ghiglia, "New approach to strip-map SAR autofocus," in *Proc. 6th IEEE Digital Signal Process. Workshop*, 1994, pp. 53–56.

[13] D. W. Hawkins, "Synthetic aperture imaging algorithms: With application to wide bandwidth sonar," Ph.D. dissertation, Dept. Electr. Electron. Eng., Univ. Canterbury, Christchurch, New Zealand, 1996.

[14] H. J. Callow, "Signal processing for synthetic aperture sonar image enhancement," Ph.D. dissertation, Dept. Electr. Electron. Eng., Univ. Canterbury, Christchurch, New Zealand, 2003.

[15] J. T. Christoff, C. D. Loggins, and E. L. Pipkin, "Measurement of the temporal phase stability of the medium," *J. Acoust. Soc. Amer.*, vol. 71, no. 6, pp. 1606–1607, Jun. 1982.

[16] P. T. Gough and D. W. Hawkins, "Imaging algorithms for a strip-map synthetic aperture sonar: Minimizing the effects of aperture errors and aperture undersampling," *IEEE J. Ocean. Eng.*, vol. 22, no. 1, pp. 27–39, Jan. 1997.

[17] M. Soumekh, *Fourier Array Imaging*. Englewood Cliffs, NJ: Prentice-Hall, 1994.

[18] C. E. Cook and M. Bernfeld, *Radar Signals: An Introduction to Theory and Application*. New York: Academic, 1967.

[19] M. Born and E. Wolf, *Principles of Optics: Electromagnetic Theory of Propagation, Interference, and Diffraction of Light*. New York: Pergamon, 1975.

[20] J. D. Lathrop and I. C. Paustian, "The defocusing of long-range synthetic aperture sonar images due to errors in either the assumed speed of sound or the assumed forward speed," 2006, unpublished.

[21] D. C. Brown, D. A. Cook, and J. E. Fernandez, "Results from a small synthetic aperture sonar," in *Proc. MTS/IEEE Oceans*, Boston, MA, 2006, pp. 1–6.

[22] M. A. Richards, "Coherent integration loss due to white Gaussian phase noise," *IEEE Signal Process. Lett.*, vol. 10, no. 7, pp. 208–210, Jul. 2003.

[23] A. Papoulis, *Probability, Random Variables, and Stochastic Processes*. New York: McGraw-Hill, 1984.

[24] A. Bellettini and M. A. Pinto, "Theoretical accuracy of synthetic aperture sonar micronavigation using a displaced phase-center antenna," *IEEE J. Ocean. Eng.*, vol. 27, no. 4, pp. 780–789, Oct. 2002.

Daniel A. Cook (M'07) received the B.S. and M.S. degrees in mechanical engineering and the M.S. degree in electrical and computer engineering from the Georgia Institute of Technology, Atlanta, in 1998, 2000, and 2007, respectively.

From 2000 to 2007, he was with the Naval Surface Warfare Center, Panama City, FL, where he developed techniques for synthetic aperture sonar motion estimation and compensation. Currently, he is with the Sensors and Electromagnetic Applications Laboratory, Georgia Tech Research Institute (GTRI/SEAL), where his research is in the area of SAR imaging and adaptive radar signal processing.

Daniel C. Brown received the B.S. degree in physics from Rhodes College, Memphis, TN, in 1999 and the M.S. degree in physics from the University of Mississippi, University, in 2003.

While at the University of Mississippi, he was part of the Thermoacoustics Research Group at the National Center for Physical Acoustics. From 2003 to 2007, he was with the Naval Surface Warfare Center, Panama City, FL, focusing on both high- and low-frequency SAS as well as interferometric SAS. Currently, he is with the Sonar Research and Development Department, Applied Research Laboratory, The Pennsylvania State University, State College, where he continues his SAS research.